Effect of microstructure on magnetic properties and anisotropy distributions in Co/Pd thin films and nanostructures

Justin M. Shaw, Hans T. Nembach, T. J. Silva, and Stephen E. Russek
Electromagnetics Division, National Institute of Standards and Technology, Boulder, Colorado 80305, USA

Roy Geiss
Materials Reliability Division, National Institute of Standards and Technology, Boulder, Colorado 80305, USA

Christopher Jones and Noel Clark
Department of Physics, University of Colorado, Boulder, Colorado 80309, USA

Titus Leo and David J. Smith
Department of Physics, Arizona State University, Tempe, Arizona 85287, USA
(Received 25 September 2009; published 19 November 2009)

The structure of Co/Pd multilayers has a strong effect on the localized anisotropy distribution within a film and on the resulting switching properties of nanostructures fabricated from identical material. By varying the underlying seed layer in sputtered films, the microstructure can be controlled from being highly (111) textured to having a random grain orientation. We find a strong correlation between the lateral homogeneity of grain orientations and the localized anisotropy distribution in the material. X-ray diffraction and reflectivity indicate that the interface is better defined and more uniform in the textured case, consistent with the presence of a strong interfacelike anisotropy.

DOI: 10.1103/PhysRevB.80.184419 PACS number(s): 75.75.+a, 75.50.Ss, 75.70.Cn, 75.30.Gw

I. INTRODUCTION

Perpendicularly magnetized nanostructures are central to many developing technologies including bit-patterned media (BPM),[1] magnetic random access memory,[2] and spintronics devices. These technologies all rely on producing arrays of perpendicularly magnetized nanomagnets with predictable switching fields and narrow switching field distributions (SFDs). An understanding of how to control and reduce SFDs is necessary before new technologies can utilize such perpendicular magnetic nanostructures. As an example, simulations of bit error rates in BPM were found to be highly dependent on anisotropy distributions,[3] which will likely have to be reduced below 5%.[4] Multilayered materials such as Co/Pd, Co/Pt, and Co/Ni are being explored for applications in BPM (Refs. 1 and 5–10) and spintronics[2] due to their highly tunable perpendicular anisotropy. While there are several factors that affect switching field distributions, such as lithographic variations and dipole interactions,[11] the dominant contribution in such materials resides in the intrinsic material properties.[12–14] More specifically, thin films, such as Co/Pd or Co/Pt multilayers, possess a lateral distribution of local anisotropy fields. When patterned into nanostructures, this distribution of anisotropy fields results in a distribution of nucleation fields from nanostructure to nanostructure. The origins of these local anisotropy fluctuations are not well understood but some evidence has suggested that variations in localized strain or grain crystal orientation may be responsible.[13–15]

We have previously shown that we could dramatically change the SFDs in nominally identical Co/Pd multilayer structures by varying the seed layer.[13] That work concluded that variations in one or more material properties were dominating SFDs in the resulting nanostructures. However, we were unclear what specific properties were primarily responsible. In the present work, we show that the choice of the underlying seed layer strongly affects the resulting microstructure, and then correlate the structure to the magnetic properties of the thin films and nanostructures. We present strong evidence that the grain orientation affects the local anisotropy field.

II. EXPERIMENT

Co/Pd multilayers were deposited by dc-magnetron sputtering on thermally oxidized Si wafers with the following structure: seed layer/$[\mathrm{Co}(t_{\mathrm{Co}})/\mathrm{Pd}(2.9t_{\mathrm{Co}})]\times 8/\mathrm{Pd}(3\ \mathrm{nm})$, where t_{Co} is the individual Co layer thickness. The seed layer was either a single Pd(3 nm) layer or a Ta(3 nm)/Pd(3 nm) bilayer. These seed layers will be referred to as the Pd *seed* and the Ta *seed*, respectively. Film deposition rates were calibrated by use of a profilometer that was itself first calibrated to within 5% of a standard. The magnetic properties of the resulting thin films were characterized using a superconducting quantum interference device (SQUID) magnetometer that was calibrated using a NIST traceable Ni sphere standard and an alternating gradient magnetometer.

Nanostructures were fabricated using electron-beam lithography to expose a polymethylmethacrylate layer which was developed in methyl isobutyl ketone MIBK: isopropanol (1:3). Approximately 20 nm of ion-beam-deposited Cr was then lifted off to form an etch mask. The patterned etch mask was then transferred to the Co/Pd multilayer thin films via a 300 eV Ar ion mill. Figure 1(a) shows a scanning electron microscope (SEM) image of typical nanostructures resulting from this process.

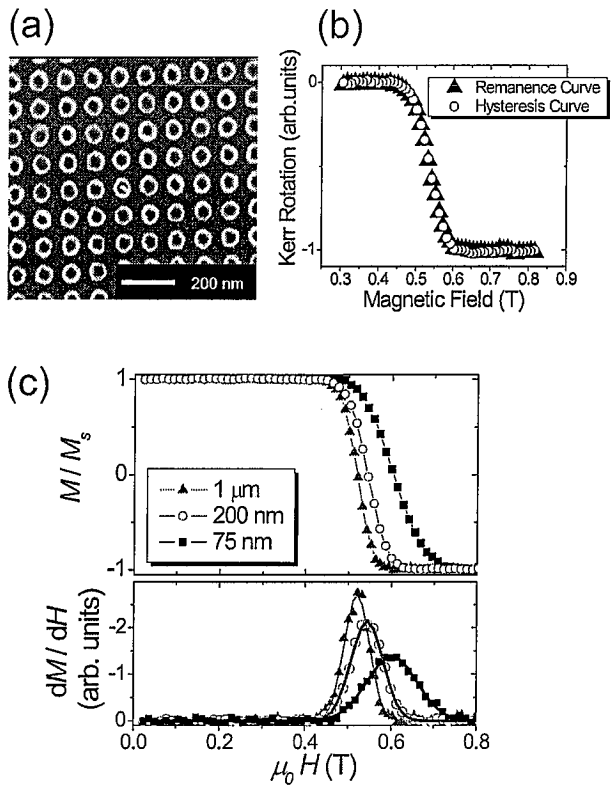

FIG. 1. (Color online) (a) SEM micrograph of the t_{Co} =0.29 nm, Pd seed sample showing nominal 50-nm-diameter nanostructures. (b) Overlaid hysteresis and remanent hysteresis curves showing identical results with either technique. (c) Hysteresis curves and resulting differential curves for various diameter structures. The lines through the differential data are Gaussian distribution fits used to extract values of H_{sf} and σ.

The magnetic properties of the nanostructures were measured by a focused polar magneto-optic Kerr effect magnetometer capable of 2 T out-of-plane fields and an approximate 15 μm spot size. Both hysteresis curves and remanent hysteresis curves were measured with this system. However, we found no difference in the two curves used in this study, as demonstrated in Fig. 1(b). We note that these two measurements may not necessarily be equivalent when the applied field is not collinear with the sample normal (i.e., when the applied field can significantly rotate the magnetization away from its remanent state or anisotropy axis). The switching field distribution (SFD) is determined by numerically differentiating the hysteresis curve and fitting it to a Gaussian distribution, as demonstrated in Fig. 1(c). This fit yields values of the average switching field, H_{sf}, and standard deviation, σ. The SFD is then calculated as: $(\sigma/H_{sf})\times 100\%$.

Surface-topography measurements were performed using tapping-mode atomic force microscopy (AFM). The grain size was determined from power spectrum plots taken from 500×500 nm^2 scans. A peak in the power spectrum was observed at the characteristic length associated with the grain size, which was verified by manually measuring several individual grains. Error bars are determined by the width of this peak, which is also related to the spread in grain sizes.

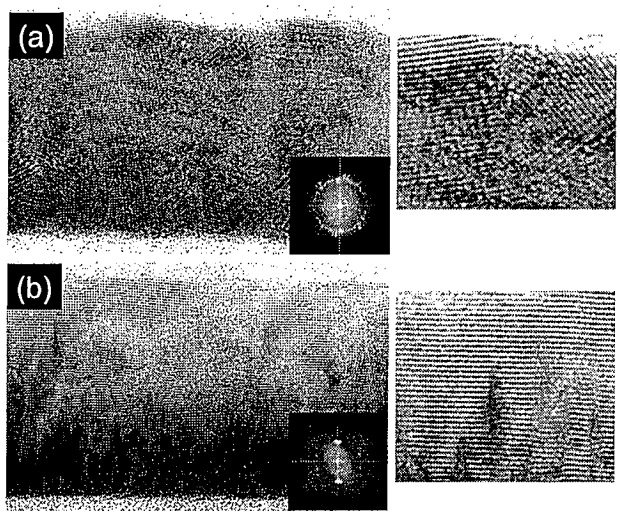

FIG. 2. Cross-section HR-TEM micrographs of: (a) Pd seed and (b) Ta seed multilayer film. Higher magnification images are included (right) as well as the corresponding Fourier transforms of the micrographs (insets).

Root-mean-square (rms) roughness values were calculated from the same scans. We caution against overinterpreting absolute numbers for the rms roughness and spread in grain size with this technique since different values can result depending on cantilever tip radius and scan parameters. However, these values prove useful for direct comparison.

Cross-section samples suitable for electron microscopy observation were prepared by slicing, mechanical polishing, and final thinning to perforation using an argon ion-mill operated at low incidence angle and low energy. Observations were made with a 400 keV high-resolution electron microscope operated in both diffraction-contrast and high-resolution imaging modes. The [110] zone axis projection of the Si(001) substrate was used to ensure that the substrate surface plane was aligned to be parallel to the incident-beam direction.

X-ray diffraction (XRD) and reflectometry (XRR) experiments were carried out on beamline X10A at the National Synchrotron Light Source, Brookhaven National Laboratories. The samples were mounted in the reflectivity geometry on a four-circle goniometer, with a germanium [111] analyzer crystal followed by a point detector mounted on the 2θ arm. This setup gives a machine angular resolution of q_{res} $<3\times 10^{-3}$ nm^{-1}. Flatness of the sample and zero for 2θ were determined, and the sample was blocking exactly half the beam when θ and 2θ were zero. The goniometer was then moved to higher q, where θ and χ angles were rocked to ensure proper zero for both angular dimensions. With all four circles aligned, measurements were made in a progression of decreasing attenuation as q was increased, allowing for eight decades in the measured intensity.

III. RESULTS AND DISCUSSION

A. Thin-film multilayer structure

Figures 2(a) and 2(b) show cross-section high-resolution

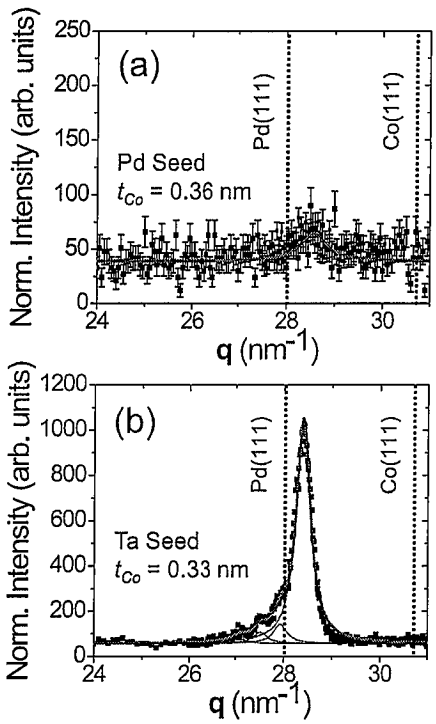

FIG. 3. (Color online) Specular XRD spectra and best fits for: (a) Pd seed and (b) Ta seed multilayer films. The ideal locations of the (111) Pd and (111) Co peaks are indicated by the vertical lines.

transmission electron microscope (HR-TEM) images for the Pd seed and Ta seed thin film samples, respectively. The images are Fourier transformed and the corresponding Fourier spectra are shown in the respective insets. A circular pattern is visible in the Fourier spectrum for the Pd seed sample, indicative of the microstructure having a highly random or nonpreferred orientation. In contrast, the Fourier spectrum for the Ta seed shows two intense spots above and below the origin which is indicative of a highly (111)-textured microstructure. Observations of the lattice fringes in the HR-TEM images are consistent with this trend.

The difference in microstructure is further confirmed in the specular XRD spectra shown in Fig. 3. Here, the scattering wave vector q is strictly normal to the surface, and thus diffraction is observed only from lattice vectors orientated normal to the surface. The Pd seed sample shows a very weak peak near the expected position of the (111) peak, consistent with a highly random distribution of grain orientation observed in the TEM data. As expected from the HR-TEM results, the Ta seed sample has a well-defined and intense (111) diffraction peak.

The peak locations for the bulk values of Co and Pd are separately indicated in Fig. 3 (vertical dashed lines); these do not coincide with the measured peaks. In addition, only a single peak is observed, suggesting that the Co/Pd layer is uniformly strained, consistent with previous observations.[16,17] Fitting of the XRD data indicates that the location of the (111) peak is 28.5 ± 0.15 nm^{-1} for the Pd seed layer and 28.4 ± 0.05 nm^{-1} for the Ta seed layer. The shoulder present on the left side of the peak is due to oscillations resulting from interference of the highly coherent x-ray beam with the multilayer film, and should not be mistaken for variations in lattice constant within the material. These oscillations have a well-defined period and were included in the peak fitting.

The lattice constant of an ideal, uniformly strained Co/Pd layer can be calculated by considering the weighted average of lattice constants for the Co and Pd present in the film. This calculation includes the Pd contained in both the seed and the capping layers, and assumes a linear relationship of lattice constants in the weighted average. Since the Ta layer is amorphous (no ordering was detected in the HR-TEM or XRD data), it was not included in the strain calculation. The calculated wave vectors for the (111) diffraction peak are q_{111}=28.42 and 28.40 nm^{-1} for the Pd seed and Ta seed samples, respectively. These values are in good agreement with the experimental data, which is consistent with a uniformly strained film. For comparison, if the average lattice constant in the Co/Pd multilayer alone is considered (neglecting the Pd in both the seed and capping layers), the calculated wave vectors become q_{111}=28.62 nm^{-1} for both the Pd seed and Ta seed samples, which is not in good agreement with the experimental data.

Ex situ AFM analysis was performed to approximate and compare the grain size and rms roughness of the multilayered films. AFM images for a few values of Co layer thickness t_{Co} for Ta [Figs. 4(a) and 4(b)] and Pd seed [Figs. 4(c) and 4(d)] samples. Plots of the grain size and rms roughness as a function of t_{Co} are given in Figs. 4(e) and 4(f) as determined from analysis of the AFM scans. Both the grain size and the rms roughness are similar for the thinnest samples. However, the Pd seed samples show a significantly larger increase in the grain size and rms roughness as t_{Co} is increased relative to the Ta seed samples.

Figures 5(a) and 5(b) show the XRR spectra for the Pd and Ta seed samples, respectively. Because of the large coherence length of the x-ray beam (~50 μm), the reflectivity curves are an effective probe of deviations of interface structure from being atomically smooth and perfectly planar. Thus, the scattering profile was modeled using tabulated bulk scattering and x-ray index of refraction constants and fits were performed whereby the thickness and interface sigma of each layer were allowed to vary. The scattering profiles for the best fits to the data are included as insets in the respective figures. The bilayer thickness was found to be approximately 10% larger relative to the thickness determined from deposition rates calibrated using a profilometer. We speculate that this discrepancy is due to the use of bulk scattering and index of refraction constants in the fits. Thus, these constants may not be strictly accurate for the ultrathin layers in the Co/Pd multilayers where some alloying may occur, as well as the presence of significant strain, as indicated by the specular XRD data.

The values of interface sigma from the fitted data were found to be (0.57 ± 0.02) and (0.35 ± 0.04) nm for the Pd and Ta seed samples, respectively. This difference is indicative of either: (i) an increase in interface roughness, (ii) lateral variations over small length scales, (iii) discontinuity of the interface, or (iv) a more diffuse interface. The AFM data show a similar trend in roughness values with a 38% in-

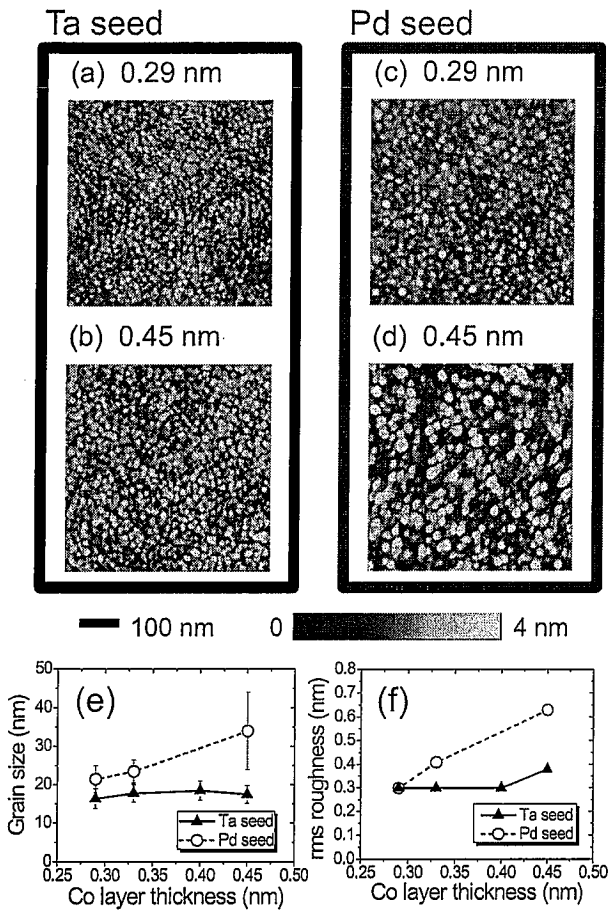

FIG. 4. (Color online) AFM images of: [(a) and (b)] Ta seed and [(c) and (d)] Pd seed multilayer films. The (e) grain size and (f) rms roughness are also plotted as a function of Co layer thickness.

crease in the Pd seed versus the Ta seed. However, the increase is not as large as the XRR data which shows a 63% increase in interface sigma of the Pd seed. These results suggest that the Ta seed sample also has a better defined, less diffuse interface and/or reduced lateral variation relative to the Pd seed sample. This trend was also qualitatively observed in the superlattice peak of the XRR spectra, as indicated by the arrows in Fig. 5. The superlattice peak is barely visible in the Pd seed spectrum, but is well defined in the Ta seed spectrum. The presence of the superlattice peak alone also verifies that the individual Co and Pd layers are well defined despite being only a few monolayers thick.

One possible explanation for the difference in interface quality could reside in an anisotropic growth mode of the system. The growth mode of epitaxial films was previously observed to be dependent on the orientation.[18] In the present case, the random orientation of the Pd seed layer sample may result in lateral variation in the growth mode and the resulting morphology changes from grain to grain.

B. Magnetic properties of multilayer films

1. Magnetization

The effective anisotropy field H_k^{eff} and saturation magnetic moment μ_s of the films were determined from in-plane

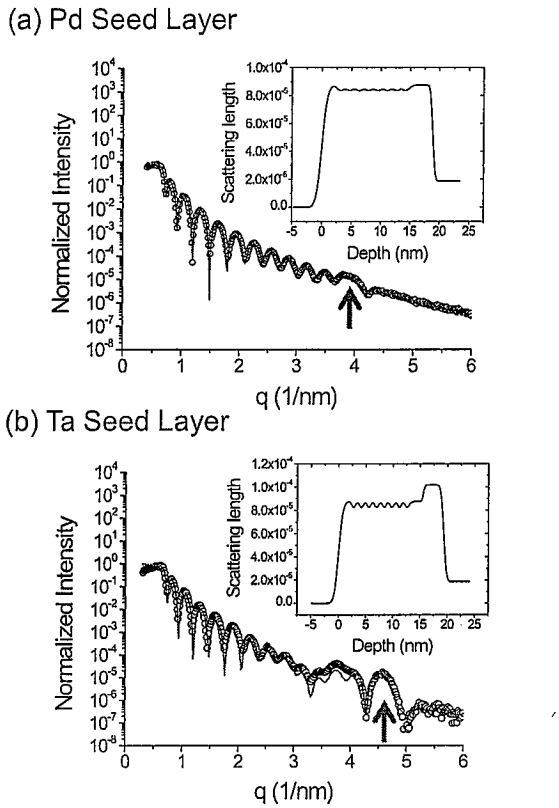

FIG. 5. (Color online) XRR spectra and best fits for: (a) Pd seed and (b) Ta seed multilayer films. The scattering profile generated by the best fits are included as insets to the respective spectra.

magnetization loops as shown in Fig. 6. The saturation magnetization M_s is calculated from $M_s=\mu_s/(a\cdot\Gamma)$, where μ_s is the saturation moment, $\Gamma=8\times(t_{Pd}+t_{Co})=8\times(3.9t_{Co})$ is the total multilayer film thickness, t_{Co} is the individual Co layer thickness, $t_{Pd}(=2.9t_{Co})$ is the individual Pd layer thickness, and a is the surface area of the sample. A plot of M_s versus the inverse Co thickness $(1/t_{Co})$ is given in Fig. 7(a). An important feature of this plot is the nonzero slope showing the effect of the magnetic polarization of Pd in the vicinity of the Co.

If the Pd polarization is assumed to be confined to the interfacial region then a simple model can be generated to

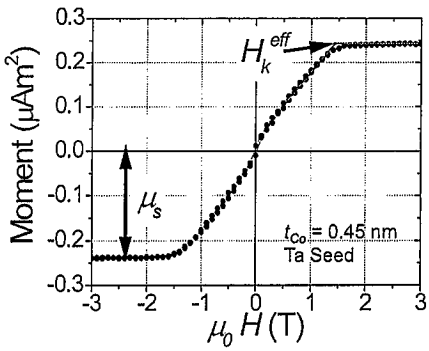

FIG. 6. (Color online) Typical SQUID in-plane magnetization curve showing how the saturation moment and effective anisotropy field are determined.

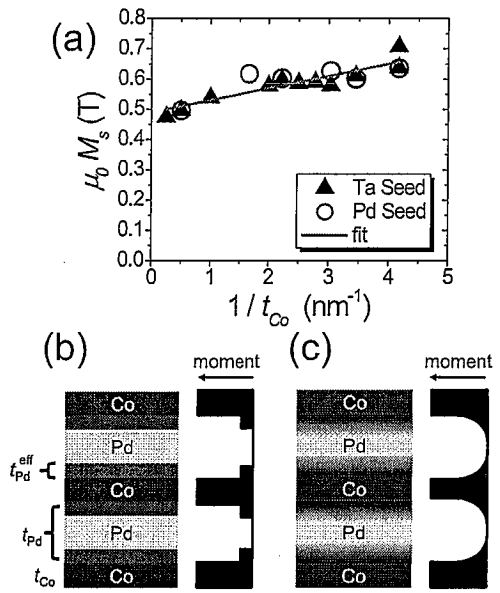

FIG. 7. (Color online) (a) Saturation magnetization as a function of inverse Co layer thickness for Pd seed (O) and Ta seed (▲) samples. A linear fit to the combined data is included which was used to determine the amount of Pd magnetic polarization. An ideal (b), and more realistic (c), schematics of the magnetic moment distribution with magnetic polarization of the interfacial Pd atoms are also shown.

explain the data and to quantify the Pd polarization. Here, we consider a thin-polarized Pd region at the Co/Pd interface with uniform magnetization M_s^{Pd} which is confined to a thickness t_{Pd}^{eff} as shown schematically in Fig. 7(b). The measured value of the total film M_s is then a sum of the Co contribution (first term) and the polarized Pd (second term) in

$$\mu_0 M_s = \frac{\mu_0 M_s^{\mathrm{Co}}}{3.9} + \frac{n\mu_0 (M_s^{\mathrm{Pd}} t_{\mathrm{Pd}}^{eff})}{\Gamma} = \frac{\mu_0 M_s^{\mathrm{Co}}}{3.9} + \frac{2\mu_0 (M_s^{\mathrm{Pd}} t_{\mathrm{Pd}}^{eff})}{3.9 t_{\mathrm{Co}}}, \tag{1}$$

where, M_s^{Co} is the bulk magnetization of Co, $n=16$ is the number of Co/Pd interfaces, and the factor of 3.9 in the first term arises from the dilution of the Co moment with Pd in the multilayer. A linear fit to the inverse thickness $(1/t_{\mathrm{Co}})$ dependence of M_s allows separate determination of M_s^{Co} and the product $(M_s^{\mathrm{Pd}} t_{\mathrm{Pd}}^{eff})$. Here, the $(M_s^{\mathrm{Pd}} t_{\mathrm{Pd}}^{eff})$ term acts as an *effective* interface magnetization term for the polarized Pd. Our data yield values of (1.86 ± 0.08) T for $\mu_o M_s^{\mathrm{Co}}$ (which is within experimental error of the tabulated value of 1.78 T for Co), and $(7.8 \pm 1.0) \times 10^{-11}$ T m for $\mu_o (M_s^{\mathrm{Pd}} t_{\mathrm{Pd}}^{eff})$. Some evidence suggests that the polarization is confined to the first 2 monolayers (0.448 nm) of Pd.[19] This would result in an average value of $\mu_o M_s^{\mathrm{Pd}} \approx 0.17$ T for the polarized Pd, which is a significant contribution the total moment profile in the system.

This analysis also shows that an interface model is consistent in describing the data in Fig. 7(a). As a consequence of such an interface effect, variations in the interface definition will also lead to variations in the local magnetization of the system. However, the data in Fig. 7(a) show that there is no significant difference in M_s with the seed layers used, and thus with the resulting microstructure. This is surprising since the XRR results indicated different interface quality in the two samples. It would be expected that a more diffuse interface would lead to more Pd atoms in contact with Co atoms, increasing the total amount of polarization. This suggests that lateral variation is responsible for the weaker superlattice peak in the XRR data of the Pd seed sample as opposed to increased interface diffusion.

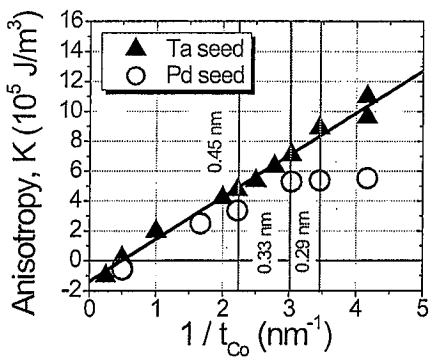

FIG. 8. (Color online) Plot of anisotropy energy density as a function of the inverse Co layer thickness for Pd seed (O) and Ta seed (▲) samples. A linear fit to the Ta data is included, which is used to separate the K_{bulk} and K_{int}. The three values of t_{Co} that were patterned into nanostructures are indicated in the figure by vertical lines.

Finally, we point out that the actual distribution of the Pd moment is likely to be highest at the first monolayer in contact with Co and then decay as the distance from the interface increases, as schematically depicted in Fig. 7(c). If $M(x_{\mathrm{Pd}})$ is taken as an arbitrary profile of the Pd magnetization as a function of distance from the interface x_{Pd}, such a magnetization profile in Pd can be related to the experimentally measured value of $(M_s^{\mathrm{Pd}} t_{\mathrm{Pd}}^{eff})$ by the following relation:

$$\mu_0 (M_s^{\mathrm{Pd}} t_{\mathrm{Pd}}^{eff}) = \int \mu_0 M(x_{\mathrm{Pd}}) dx_{\mathrm{Pd}} = (7.8 \pm 1.0) \times 10^{11} \text{ T m} \tag{2}$$

2. Magnetic anisotropy

The effective anisotropy field H_k^{eff} is determined from the saturation point of in-plane magnetization curves as shown in Fig. 6. For the analysis here, second-order anisotropy terms are neglected. The intrinsic anisotropy energy density (K^{film}) normalized to the volume of the entire multilayer film is then determined from Eq. (3).

$$K^{film} = \left(\frac{\mu_0 M_s}{2}\right)(H_k^{eff} + M_s). \tag{3}$$

The anisotropy energy density is plotted as a function of $1/t_{\mathrm{Co}}$ in Fig. 8 for both the Pd and Ta seed layer samples. The Ta seed layer data show a linear trend as would be expected if the anisotropy is due to a bulk (K_{bulk}) and an

interfacial (K_{int}) contribution. K_{bulk} and K_{int} are related to the total anisotropy and can be separated by the following relation:

$$K^{film} = K_{bulk} + \frac{nK_{int}}{\Gamma} = K_{bulk} + \frac{2K_{int}}{3.9t_{Co}}. \quad (4)$$

The negative value of the y intercept in Fig. 8, and thus K_{bulk}, indicates that this term favors in-plane magnetization. As a result, the out-of-plane anisotropy originates from K_{int}. There is still significant debate as to whether this originates fundamentally from an intrinsic interface anisotropy, interface alloying, or from magnetoelastic origins.[6,19–23] However, since we keep the ratio t_{Pd}/t_{Co} fixed at 2.9 and the x-ray data indicate the multilayer is uniformly strained, the magnetoelastic contribution would be constant for the multilayers studied here, and should therefore be included in the K_{bulk} term. While such a magnetoelastic contribution to K_{bulk} cannot be excluded, our data are consistent with the presence of a strong out-of-plane interfacial-like anisotropy. Although beyond the scope of the present work, it is reasonable to assume that both magnetoelastic and interfacial anisotropies are present and contribute to K_{film}, which could resolve the controversy and the evidence for the existence of both.

In contrast to the textured Ta seed anisotropy data, the randomly oriented Pd seed shows very different behavior that is not well described by Eq. (4). At smaller thickness values (below $t_{Co} \approx 0.33$ nm), the anisotropy appears to be strongly suppressed relative to the Ta seed data. However, the data begin to align with the Ta seed data at larger thickness values. This is consistent with the XRR data, which show a less defined or consistent interface in the Pd seed sample. Because suppression of the anisotropy is present only below a certain thickness, these data suggest that the Co/Pd interface may not be as laterally continuous or homogeneous below this thickness. Differences in the anisotropy between the (111)-textured and random orientations would be expected since K_{bulk} was found to be a function of orientation,[20] but such effects would be expected to be independent of thickness.

If the anisotropy is assumed to reside solely in the Co layers and interface (i.e., neglecting contributions of the polarized Pd) then the *intrinsic* anisotropy energy density (K) for the Ta seed data can be approximated by replacing M_s with M_s^{Co} and Γ with the *total* Co thickness, nt_{Co}, in Eqs. (3) and (4). (Recall that K^{film} in Eq. (4) is an energy density treating the entire film as a homogeneous system. Here, we find the *intrinsic* energy density assuming it resides solely in the Co layers and normalizing it to Co. While K^{film} normalized to the entire multilayer film volume is more useful in many applications, this treatment is more fundamental and allows for direct comparison of results regardless of the multilayer thickness structure). This analysis yields values of -7.4×10^5 J/m^3 for the bulk anisotropy and 6.8×10^{-4} J/m^2 for the interface anisotropy energy. The measured interface anisotropy agrees well with the value of 6.3×10^{-4} J/m^2 measured by Engel *et al.*[20] despite very different growth conditions. The values of the bulk anisotropy energy in these cases are not directly comparable since the ratio of t_{Co} to t_{Pd} differ. Recall, that the x-ray diffraction results indicate a uniformly strained film, and by varying this ratio, the magnetoelastic contribution to K_{bulk} will also vary. In addition, Engel *et al.* found a profound difference in K_{bulk} as a function of crystal orientation further complicating direct comparison.

This analysis shows that the interfacelike anisotropy K_{int} term is very large in magnitude and as a result, the anisotropy is a strong function of the Co and Pd layer thickness. Thus, small lateral variations in layer thickness will result in significant local variations in the anisotropy. Such thickness fluctuations could result from film roughness as well as differences in the growth mode from grain to grain due to variations in crystallographic orientation. This latter effect would offer additional dependence of the local anisotropy field on the grain orientation relative to the more obvious contribution of the magnetocrystalline anisotropy.

Finally, it would be expected that a deviation from linearity in Eq. (4) would occur at the point where the transition from fcc to hcp Co occurs. Such a transition was previously observed to occur at $t_{Co}=1.5$ nm in Co/Pt multilayers.[5] Evidence of this transition in the anisotropy data is not observed here, indicating that its effect on the total anisotropy is relatively small. Thus, lateral fluctuations from fcc to hcp Co are unlikely to cause a large effect on anisotropy variations.

C. Switching properties of nanostructures

The multilayer thin films described in the previous sections were patterned into circular structures ranging from 50 nm to 5 μm in diameter. Figures 9(a)–9(c) show the diameter dependence of the average switching field H_{sf} for samples with $t_{Co}=0.29$, 0.33, and 0.45 nm, respectively. One trend observed in all samples was that the textured Ta seed data have significantly higher values of H_{sf} relative to the randomly oriented Pd seed data. This trend can be easily explained in the data for $t_{Co}=0.29$ and 0.33 nm because of the detectable difference in anisotropy between the multilayered films (Fig. 8). However, while the film anisotropies are more similar for the case of $t_{Co}=0.45$ nm, the values of H_{sf} remain significantly different. A full explanation will probably require an accounting of the random orientation of the Pd seed layer, which would contribute to a much larger distribution of localized anisotropy fields. This effect of anisotropy distribution on the switching field is outlined in Ref. 12. It would also be expected that a larger distribution of anisotropy fields would result in larger switching field distributions in patterned structures. Indeed, when the SFDs are compared in Fig. 9(f), the Pd seed sample has a significantly larger value relative to the Ta seed sample, especially in the smallest structures, confirming a significant increase in anisotropy distributions.

Two interesting trends in the SFD data are also observed in Figs. 9(d)–9(f): (1) the textured Ta seed data are largely unchanged as t_{Co} is varied and (2) the SFDs significantly decrease for the randomly oriented Pd seed data as the t_{Co} is decreased. These trends correlate well with the grain size and rms roughness data, which show little difference over this thickness range for the Ta seed, but a large increase in the Pd

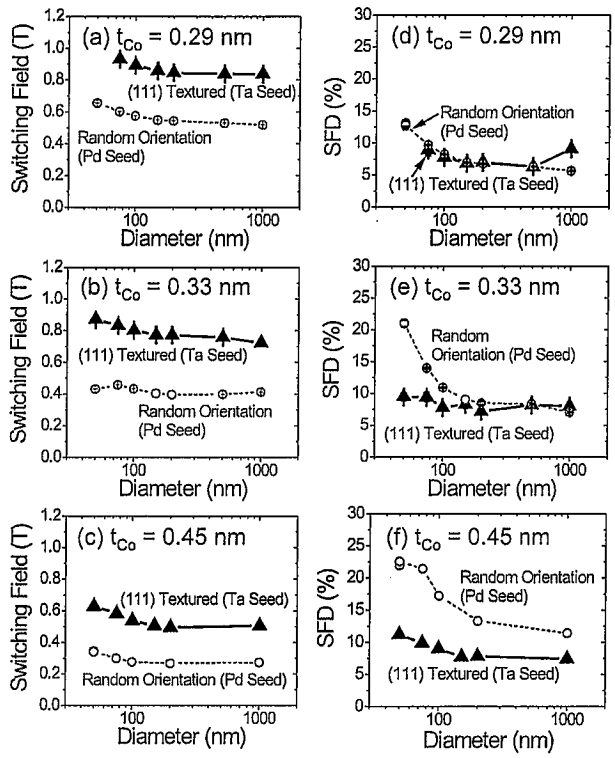

FIG. 9. (Color online) Plots of H_{sf} as a function of nominal nanostructure diameter for (a) t_{Co}=0.29 nm, (b) t_{Co}=0.33 nm, and (c) t_{Co}=0.45 nm samples, as well as plots of SFD as a function of nominal nanostructure diameter for (d) t_{Co}=0.29 nm, (e) t_{Co} =0.33 nm, and (f) t_{Co}=0.45 nm samples with both Pd seed (O) and Ta seed (▲).

seed for larger thicknesses. However, grain size and roughness cannot be the sole contribution to the switching properties since the difference in H_{sf} remains large between the Pd seed and Ta seed sample even when the grain size and roughness values are similar as is the case for t_{Co}=0.29 nm.

These results suggest that the random grain orientation may affect switching properties in nanostructures through multiple processes: (1) the grain orientation directly affects the anisotropy of individual grains (and thus, anisotropy distribution across a thin film) via magnetocrystalline and/or interfacial anisotropy effects. Additional evidence of this effect was reported by Lau *et al.*[14] who identified nanostructures with lower switching fields statistically contained a "trigger" grain with an orientation that deviated from (111) and (2) the grain orientation affects the film morphology, grain size, and roughness, which is consistent with previous work by Przybylski *et al.*[18] that showed different growth modes as a function of orientation. By definition, roughness represents a lateral inhomogeneity in the thin film and would be expected to increase inhomogeneity of the magnetic properties. The grain size, however, would influence the switching properties via a statistical process. Since a nanostructure contains a finite number of grains, the smaller the grains, the more averaging of the magnetic properties occurs. This is why the SFDs are seen to increase as the diameter of the nanostructure decreases; larger structures average over all the possible variations in grain properties whereas small structures are dominated by the properties of only a few grains. As a result, larger grains would be expected to produce larger SFDs since nanostructures would contain fewer grains. As an example, a 50 nm nanostructure would ideally contain 11 grains of size 15 nm but only 2–3 grains of size 30 nm significantly reducing averaging effects.

Finally, while the defects and/or properties which control both H_{sf} and SFDs in nanostructures cannot be fully separated, we clearly show strong evidence that grain orientation directly affects local anisotropy distributions, as well as indirectly affecting the magnetic properties of nanostructures by means of roughness and/or grain size. The picture is further complicated since effects of edge damage from the ion-milling process are not considered.[24] However, while such effects complicate quantitative modeling, the edge damage effects will be the same for all samples studied in this work allowing for comparative analysis. With this in mind, it is reasonable that all of these factors contribute and may have greater or lesser influence depending on the thickness regime. However, our data clearly indicates that generating a homogenous distribution of grain orientation results in a significantly more predictable anisotropy and lower distribution of anisotropy fields in nanostructures.

IV. CONCLUSIONS

We have shown that grain orientation plays a significant, if not dominant, role in controlling anisotropy distributions in perpendicularly magnetized Co/Pd nanostructures. Comparison of nominally identical samples with a highly textured microstructure relative to those with a random grain orientation shows a strong correlation of the microstructure to the anisotropy and SFDs. We have shown that the microstructure can be substantially altered with the use of seed layers. In the case of a Pd seed, the microstructure is highly random in crystallographic orientation whereas a highly (111)-textured structure is produced from a Ta seed layer. A resulting decrease in anisotropy distributions is achieved with such a (111) texture, which was shown to produce a more laterally consistent Co/Pd interface. In this case, the thickness dependence of the anisotropy shows a strong interfacelike contribution to the perpendicular component. Finally, no differences in amount of Pd polarization were observed despite the changes in microstructure.

ACKNOWLEDGMENTS

The authors are grateful to Philip Ryan, Bruce Terris, Tom Thomson, and Olav Hellwig for valuable discussions; Donna Hurley for use of her AFM system, and Chenhui Zhu for useful conversations relating to the x-ray work. Use of the National Synchrotron Light Source, Brookhaven National Laboratory, was supported by the U.S. Department of Energy, Office of Science, Office of Basic Energy Sciences, under Contract No. DE-AC02-98CH10886. Use of facilities in the John M. Cowley Center for High Resolution Electron Microscopy at Arizona State University is gratefully acknowledged.

[1] B. D. Terris, J. Magn. Magn. Mater. **321**, 512 (2009).
[2] S. Mangin, D. Ravelosona, J. A. Katine, M. J. Carey, B. D. Terris, and E. E. Fullerton, Nature Mater. **5**, 210 (2006).
[3] M. E. Schabes, J. Magn. Magn. Mater. **320**, 2880 (2008).
[4] H. J. Richter, J. Magn. Magn. Mater. **321**, 467 (2009).
[5] D. Weller, L. Folks, M. Best, E. E. Fullerton, B. D. Terris, G. J. Kusinski, K. M. Krishnan, and G. Thomas, J. Appl. Phys. **89**, 7525 (2001).
[6] D. J. Larson, A. K. Petford-Long, Y. Q. Ma, and A. Cerezo, Acta Mater. **52**, 2847 (2004).
[7] E. Chunsheng, V. Parekh, P. Ruchhoeft, S. Khizroev, and D. Litvinov, J. Appl. Phys. **103**, 063904 (2008).
[8] M. Abes, M. V. Rastei, J. Venuat, A. Carvalho, S. Boukari, E. Beaurepaire, P. Panissod, A. Dinia, J. P. Bucher, and V. Pierron-Bohnes, J. Appl. Phys. **105**, 113916 (2009).
[9] B. D. Belle, F. Schedin, N. Pilet, T. V. Ashworth, E. W. Hill, P. W. Nutter, H. J. Hug, and J. J. Miles, J. Appl. Phys. **101**, 09F517 (2007).
[10] N. Kikuchi, S. Okamoto, and O. Kitakami, J. Appl. Phys. **105**, 07D506 (2009).
[11] O. Hellwig, A. Berger, T. Thomson, E. Dobisz, Z. Z. Bandic, H. Yang, D. S. Kercher, and E. E. Fullerton, Appl. Phys. Lett. **90**, 162516 (2007).
[12] T. Thomson, G. Hu, and B. D. Terris, Phys. Rev. Lett. **96**, 257204 (2006).
[13] J. Shaw, W. Rippard, S. Russek, T. Reith, and C. Falco, J. Appl. Phys. **101**, 023909 (2007).
[14] J. W. Lau, R. D. McMichael, S. H. Chung, J. O. Rantschler, V. Parekh, and D. Litvinov, Appl. Phys. Lett. **92**, 012506 (2008).
[15] R. Sbiaa, C. Z. Hua, S. N. Piramanayagam, R. Law, K. O. Aung, and N. Thiyagarajah, J. Appl. Phys. **106**, 023906 (2009).
[16] T. Asahi, K. Kuramochi, J. Kawaji, T. Onoue, T. Osaka, and M. Saigo, J. Magn. Magn. Mater. **235**, 87 (2001).
[17] S. Mohanan and U. Herr, J. Appl. Phys. **102**, 093903 (2007).
[18] M. Przybylski, L. Yan, J. Zukrowski, M. Nyvlt, Y. Shi, A. Winkelmann, J. Barthel, M. Wasniowska, and J. Kirschner, Phys. Rev. B **73**, 085413 (2006).
[19] H. Nemoto and Y. Hosoe, J. Appl. Phys. **97**, 10J109 (2005).
[20] B. N. Engel, C. D. England, R. A. Van Leeuwen, M. H. Wiedmann, and C. M. Falco, Phys. Rev. Lett. **67**, 1910 (1991).
[21] J. Carrey, A. E. Berkowitz, W. F. Egelhoff, Jr., and D. J. Smith, Appl. Phys. Lett. **83**, 5259 (2003).
[22] S. K. Kim, J. W. Lee, J. R. Jeong, J. Kim, and S. C. Shin, Appl. Phys. Lett. **79**, 1652 (2001).
[23] N. Nakajima, T. Koide, T. Shidara, H. Miyauchi, H. Fukutani, A. Fujimori, K. Iio, T. Katayama, M. Nyvlt, and Y. Suzuki, Phys. Rev. Lett. **81**, 5229 (1998).
[24] J. M. Shaw, S. E. Russek, T. Thomson, M. J. Donahue, B. D. Terris, O. Hellwig, E. Dobisz, and M. L. Schneider, Phys. Rev. B **78**, 024414 (2008).